Measurement of the Dispersion of Electronic Surface Excitations via Analysis of Inelastic Low-Energy-Electron Diffraction*

C. B. Duke† and U. Landman†
Department of Physics, Materials Research Laboratory and Coordinated Science Laboratory, University of Illinois, Urbana, Illinois 61801
and Xerox Research Laboratories, Xerox Square, Rochester, New York 14644
(Received 9 June 1972)

A quantum-field theory of inelastic low-energy-electron diffraction (ILEED) is applied to examine four significant limitations on the uniqueness and precision with which the dispersion relation of electronic surface excitations can be determined from a model analysis of experimental ILEED intensities. The example of surface plasmons on Al (111) is described in detail. A grid size of $\delta w \cong 0.050$ eV in the loss energy and $\delta\theta' \cong 0.5°$ in the final-state polar angle is established as being sufficiently small to provide a precise distinction between differing surface-plasmon dispersion relations, yet sufficiently large to permit the use of a two-step model of the diffraction process rather than a complete dynamical calculation in the analysis. Comparison of two-step with dynamical isotropic-scatterer inelastic-collision model calculations reveals that plots of the scattered intensity in a given exit direction as a function of the loss energy (i.e., "loss profiles") provide the most appropriate method of data presentation for theoretical analysis via a two-step model. The loss-energy ($\Delta w \sim 1$ eV) and angular ($\Delta\theta' \sim 2°$) resolution of present ILEED spectrometers is shown not to be a limiting factor of the precision of our analysis. Finally, we demonstrate that within the context of both the two-step and dynamical model calculations, the conservation laws fail to provide a sufficiently detailed description of ILEED intensities to permit a determination of the surface-plasmon dispersion from kinematical considerations alone. This dispersion can be extracted accurately from observed ILEED intensities *only* via a complete analysis of the loss profiles for various values of the incident-beam parameters using a two-step (or more complicated) model. These four results are combined to propose an analytical procedure which provides an accurate yet economical determination of the surface branches of the electronic excitation spectra of the valence-electron fluid in a solid.

I. INTRODUCTION

The principal objective of modern surface spectroscopy is the determination of the chemical, geometrical, vibrational, and electronic structure of the upper few layers of a solid in a high-vacuum environment.[1] The three major techniques for determining those features of the electronic excitation spectra associated with solid surfaces are inelastic low-energy-electron diffraction (ILEED), ion-neutralization spectroscopy (INS), and photoelectron spectroscopy (PES). This paper is devoted to an examination of the precision and accuracy of the first of these techniques with emphasis on the special case of the determination of surface-plasmon dispersion on Al (111). All three techniques require the intermediary of a microscopic theoretical model to convert experimental measurements into a quantitative parametrization of the excitation spectrum. Therefore the adequacy of these models, as well as that of the experimental measurements, determines the precision and accuracy of the characterization of the surface achieved using a given technique. Consequently, the specification of the nature and sophistication required of a model of the ILEED process is the focus of our attention herein.

The example that we use to illustrate our results is the determination of the surface-plasmon dispersion relation (SPDR) on Al (111). This SPDR, i.e., the energy and reciprocal lifetime of collective excitations of a bounded-electron fluid associated with a surface charge on the fluid,[2,3] reflects the microscopic electronic surface properties of the fluid (e.g., its charge-density profile). The problem of calculating it has been tackled by various theoretical approaches, ranging from microscopic quantum-mechanical models[4–7] to hydrodynamical[2,8,9] and semiclassical phenomenological theories.[2,3,10] Its extraction from experimental ILEED intensities, using a quantum field theory of this process,[11,12] has been discussed previously by Bagchi, Duke, and co-workers.[13–15] Our analysis is an extension of theirs in which we critically assess the selection of the data to be analyzed, the adequacy of using a two-step model[14–16] as the basis for the analysis, and the accuracy of the parameters in the resulting expression for the SPDR.

The central problem in analyzing ILEED data is the correlation between the extent of the data, the instrumental resolution, and the uniqueness with which excitation dispersion relations can be deter-

mined. Analysis of ILEED experiments on Al (111)[17] reveals that inevitable uncertainties occur in the SPDR. For example,

$$\hbar\omega_s(p_{\parallel}) = \hbar\omega_s(\pm 0.2\ \text{eV}) + C_1(\pm 2.5)p_{\parallel} + C_2(\pm 5.5)p_{\parallel}^2, \tag{1}$$

if Porteus's data for the incident-beam parameters $E \cong 50$ eV, $\theta = 15°$, $\psi = 60°$ are used as the basis for the analysis.[17-19] Confronted with such uncertainties, in this paper we examine four specific issues involved in their reduction: the magnitudes of the energy and angular grids necessary to distinguish between different SPDR's; the minimal level of theoretical sophistication required to perform the model analysis; the sort of profiles to be analyzed; and the effect of finite instrumental resolution on the results. The definition of the various "profiles" used to present the ILEED intensities is given by Larmore and Duke.[12]

The major result of our study is that the SPDR's can be determined optimally by a two-step model analysis of the *loss profiles alone* [i.e., plots of scattered intensity versus loss energy $w = E - E'$ for fixed incident-beam parameters (E, θ, ψ) and exit-angle parameters $(\theta', \psi' = \psi + \pi)$]. In this analysis we can employ any loss-energy grid $\delta w \geq 50$ meV and exit-angle grid $\delta\theta' \geq 0.5°$. The $\delta w = 50$ meV, $\delta\theta' = 0.5°$ increments are the minimal possible values compatible with the use of the two-step model and current uncertainties in the electron-solid force law. They are *independent* of the experimental resolution $(\Delta w, \Delta\theta')$ of the ILEED spectrometer provided $\Delta w \lesssim 2$ eV and $\Delta\theta' \lesssim 2°$. In the special case of Al (111), the maximal size of these grids compatible with a clear distinction between differing SPDR is $\delta w \leq 100$ meV and $\delta\theta' \leq 1°$.

We proceed by first reviewing in Sec. II the model parameters that are used in the calculations. The results of a sample analysis of Porteus's ILEED experiments on Al (111) used to determine the region of ambiguity in the SPDR are presented in Sec. III. The rest of the paper is devoted to questions associated with the reduction of the ambiguity between different SPDR's. Assuming ideal resolution, we establish in Sec. IV the necessary energy-loss grid size, discuss the effects of multiple-scattering phenomena and diffraction conditions on the positions of the peaks in the loss profiles, and describe the difficulties encountered with an analysis of angular profiles. The effects of finite resolution on the conclusions drawn in the previous sections are studied in Sec. V and those of phonon-assisted diffraction are examined in Sec. VI. Finally, we present in Sec. VII a procedure for extracting SPDR from an analysis of experimental ILEED intensities, which exhibits the merits of being economical in the amount of data to be measured and analyzed while enabling a substantial reduction of the uncertainties in the resulting dispersion relation.

II. DEFINITION OF MODEL PARAMETERS

The detailed definition of the quantum field theoretical two-step model has been described elsewhere.[11,12] Moreover, a complete derivation of the expressions for the inelastic scattering cross-sections based on an improved version of this model, which embodies a more accurate treatment of the electron interaction with the surface plasmons, has been given recently by Bagchi and Duke[15] for the isotropic-scatterer rigid-lattice version of the model. Therefore we simply recall those definitions that must be specified in order to make the results shown in the figures well defined, and present the minor extension of the isotropic-scatterer model necessary to specify our treatment of higher-partial-wave phase shifts in the electron–ion-core interaction. [Equations in Bagchi and Duke's paper[15] will be designated as BD(1), BD(2), etc.]

The elastic scattering of the electron from the solid is given in terms of a one-electron proper self-energy Σ and electron–ion-core phase shifts δ_l. The consequences of the electron-electron interactions are described by the real part of the one-electron proper self-energy ("inner potential") V_0 and the inelastic-collision damping length λ_{ee} via

$$\Sigma(E) = -V_0 - i\Gamma(E), \tag{2a}$$

$$\Gamma(E) = \frac{\hbar^2}{m\lambda_{ee}}\left(\frac{2m}{\hbar^2}(E + V_0)\right)^{1/2} \tag{2b}$$

as originally given by Duke *et al.*[20,21] We designate by $\vec{g}$ the reciprocal-lattice vectors of the (periodic) two-dimensional atomic layers parallel to the surface (out of which the solid is constructed). We let $\vec{k}$ and $\vec{k}'$ denote the electron momenta before and after scattering, their components parallel to the surface being given by $\vec{k}_{\parallel}$ and $\vec{k}'_{\parallel}$, respectively. In terms of these quantities we define the normal component of electron momentum inside the metal, associated with a beam characterized by $\vec{k}'_{\parallel} = \vec{k}_{\parallel} + \vec{g}$, via

$$k_{\perp}(\vec{g}, E) = \{2m[E - \Sigma(E)]/\hbar^2 - (\vec{k}_{\parallel} + \vec{g})^2\}^{1/2}. \tag{3}$$

The extension to the multiple-phase-shift description of the elastic scattering is achieved by replacing the isotropic scattering amplitude BD(3) by the angular-dependent partial-wave expansion of the scattering amplitude given by

$$t(\vec{k}', \vec{k}, E) = \frac{h^2}{4\pi ikm}\sum_{l=0}^{\infty}(2l+1)(e^{2i\delta_l(E)} - 1)P_l(\cos\gamma), \tag{4}$$

where $P_l(\cos\gamma)$ is the lth Legendre polynomial, γ is the scattering angle given by

$$\gamma = \pi - \theta - \theta', \tag{5}$$

and $\delta_l(E)$ are the partial-wave phase shifts obtained by Laramore and Duke[22] from Snow's APW potential.[23] The calculations presented in this paper were per-

formed using four partial waves ($l \leq 3$) for each energy.

Calculations of the inelastic scattering cross sections require that we specify the plasmon dispersion relations as well as elastic and inelastic electron-solid interaction vertices. The latter are given in BD(4–10). The bulk-plasmon dispersion is given by

$$\hbar\omega_b(p) = 14.2 + 3.048p^2, \tag{6a}$$

$$\Gamma_b(p) = 0.53 + 0.103p^2 + 1.052p^4. \tag{6b}$$

Energies are measured in eV and momenta in Å^{-1}. Except for the threshold value of 14.2, all of the parameters are obtained from keV thin-film transmission experiments as described by Bagchi and Duke.[15] For the surface-plasmon dispersion and damping, respectively, we use the forms

$$\hbar\omega_s(p_\parallel) = \hbar\omega_s + C_2 p_\parallel + C_2 p_\parallel^2, \tag{7a}$$

$$\Gamma_s(p_\parallel) = \Gamma_s + D_1 p_\parallel. \tag{7b}$$

The threshold, $\hbar\omega_s$, and the coefficients C_1, C_2, Γ_s, and D_1 are regarded as parameters to be determined by the "best fit" between the experimental and theoretical intensity profiles.

The expression for the inelastic scattering cross sections is given by

$$\left(\frac{d^2\sigma}{dEd\Omega}\right)^{(4)} = \left(\frac{d^2\sigma}{dEd\Omega}\right)^{(4)}_{sp} + \left(\frac{d^2\sigma}{dEd\Omega}\right)^{(4)}_{bp}, \tag{8}$$

where the surface and bulk contributions are given by BD(16–20), with $t(E)$ replaced by $t(\vec{k}', \vec{k}, E)$ as given in Eq. (4). Insepection of the model used by BD reveals that for loss energies (w) greater than $\hbar\omega_s$, the shape of inelastic cross sections as a function of the exit-beam parameters (w, θ') is insensitive to the form of the model used for the inelastic electron-surface-plasmon vertex. Consequently, although for our analysis in this paper we utilize the semiclassical excitation of surface plasmons as an illustrative example, our general conclusions are valid for any surface branch of the electronic excitation spectrum (i.e., branches exhibiting excitation energies which depend solely on $p_\parallel$). Of course, in each individual case the numerical work analogous to that illustrated in subsequent sections must be repeated. The methodology we use here, however, is applicable to the examination of any surface excitation.

III. ANALYSIS OF ILEED DATA: Al(111)

Since this paper is devoted to a systematic study of the precision and accuracy of a data-analysis procedure, it is appropriate to begin our presentation by recalling the definition of this procedure and illustrating the uncertainties in the dispersion relations of surface excitations to which its applications can lead.

The fundamental concept underlying the procedure[12,24] is that of exploiting a parametrization of resonances in the elastic low-energy-electron diffraction (ELEED) intensities to determine the elastic electron-solid interaction. This in turn is used in the two-step model to determine the dispersion relation of a surface excitation. We proceed by first isolating a prominent resonance in the ELEED intensities, then selecting V_0 and λ_{ee} in Eqs. (2) to "fit" this resonance, and finally using the two-step model for (E, θ, ψ) in the neighborhood of the resonance to "predict" the ILEED intensities as functionals of the surface-excitation dispersion relation, Eqs. (7). By adjusting V_0 and λ_{ee} to fit the ELEED intensities *a posteriori*, we avoid confronting the embarassing fact that they cannot be described adequately by existing microscopic models of the electron-electron interaction-induced electron-solid optical potential.[4,22] This parameter adjustment is, of course, a potential source of error in the analytical procedure. Unfortunately, we cannot check its consequences within the framework of our model and, of necessity, neglect them in our present considerations.

Another source of systematic error that we cannot examine explicitly is the functional form of the inelastic-loss vertex. Presumably, the weak dependence[15] of this vertex on $p_\parallel$ (and only on $p_\parallel$ in simple models[4]) renders errors from this origin of negligible importance.

Given the elastic and inelastic electron-solid vertex functions, however, the major factors determining the uniqueness and accuracy with which a surface-excitation dispersion relation can be extracted from measured ILEED intensities are the extent of the data and the instrumental resolution. To illustrate their effect on the surface-plasmon dispersion relations, we compare sample theoretical calculations with experimental measurements[17–18] of loss and angular profiles characterized by a mesh of 0.4 eV in the loss energy (δw) and 2° in the exit angle ($\delta\theta'$) and by an instrumental resolution of 1 eV in the loss energy and 2° in the exit angle.

For reference we present in Fig. 1 the energy profiles (plots of the scattered intensity versus incident electron energy E for fixed initial and final angular parameters, and fixed energy loss w) of the (00) beam of electrons scattered from Al (111) at an incident polar angle of $\theta = 15°$ and in an azimuthal plane with $\psi = 60°$. The elastic energy profile has maxima at $E_B = 50$ eV and $E_B = 103$ eV. The energy profiles for $w = 12$ eV, calculated with three different dispersion relations varying from a linear to a quadratic dependence on the plasmon momentum $p_\parallel$, exhibit a peak splitting of 12 eV, which corresponds to the processes of elastic diffraction before energy loss (i.e., the low-energy component

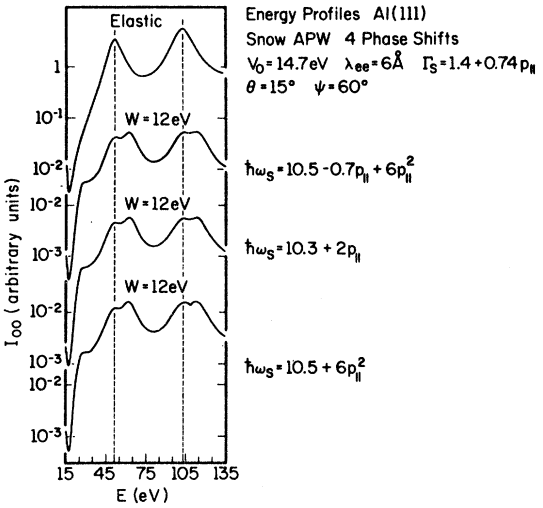

FIG. 1. Elastic ($w=0$) and $w=12$ eV energy profiles for the (00) beam of electrons scattered from Al (111) associated with three dispersion relations the coefficients of which lie in the region of ambiguity (see, e.g., Fig. 4). A four-phase-shift two-step model was used with the values of the parameters indicated in the figure. Vertical dashed lines are drawn to guide the eye in locating the positions of the primary Bragg maxima.

of the doublet which occurs at the same energy as the peak in the elastic profile) and of energy loss by the electron followed by elastic diffraction (the high-energy component occurring at E_B+w). In Fig. 2 we compare experimental and theoretical loss profiles for two angles of exit, $\theta'=20°$ and 26°. The evident agreement in peak positions between the theoretical curves corresponding to the three representative dispersion relations and the experimental profiles prevents the differentiation between the different SPDR. This conclusion holds also for the angular profiles shown in Fig. 3 for values of the loss energy ($w=8$, 10, and 12 eV) spanning the surface-plasmon peak in the loss profiles (Fig. 1).

A detailed analysis, sample calculations in which were shown above, reveals the occurrence of uncertainties in the SPDR given in Eq. (1). Such uncertainties are inevitable consequences of the finite energy and angular resolution of an ILEED spectrometer. We incorporate them into our analysis by introducing, via Fig. 4, the concept of a "region of ambiguity." This concept reflects the observation that any dispersion relation whose coefficients lie in the shaded region yields adequate agreement between the theoretical and the observed loss and angular profiles.

IV. REDUCTION OF SURFACE-EXCITATION AMBIGUITY: IDEAL RESOLUTION

Realizing the indistinguishability of a whole family of SPDR's, we next focus our attention on the conditions necessary to reduce the number of dis-

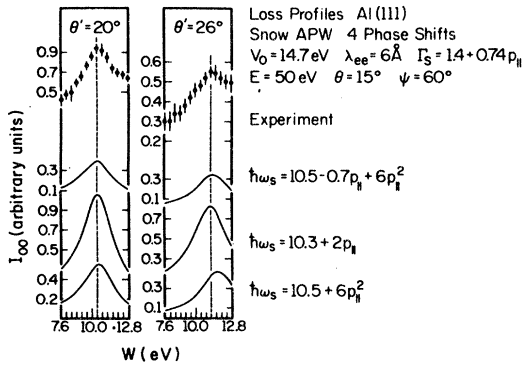

FIG. 2. Experimental and calculated loss profiles for the (00) beam of electrons scattered from Al (111) for two exit angles ($\theta'=20°$ and 26°) and primary energy $E=50$ eV. The three lower (solid) curves are the profiles corresponding to three dispersion relations the coefficients of which lie in the region of ambiguity (see, e.g., Fig. 4). The top points with error bars are the experimental results. The vertical dashed lines are drawn at values of the loss energy (w) corresponding to the peak positions in the experimental results, and indicate the agreement between the peak positions of the experimental and the calculated loss profiles for the three different dispersion relations. A four-phase-shift two-step model was used with the values of the parameters indicated in the figure.

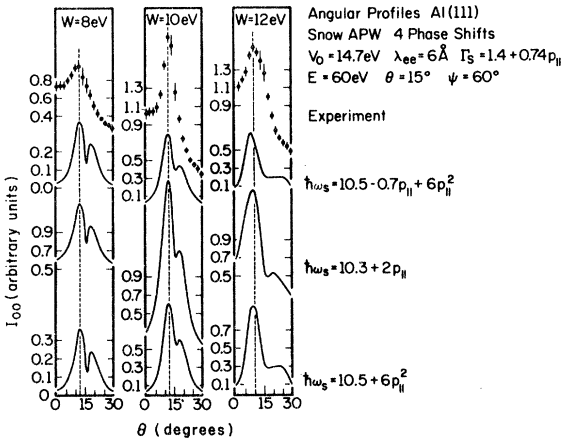

FIG. 3. Experimental and calculated angular profiles for the (00) beam of electrons scattered from Al (111) for three values of the loss energy ($w=8$, 10, and 12 eV) and primary energy $E=60$ eV. The three lower (solid) curves are the profiles corresponding to three dispersion relations the coefficients of which lie in the region of ambiguity (see, e.g., Fig. 4). The top points with error bars are the experimental results. The vertical dashed lines are drawn at values of the exit angle (θ') corresponding to the surface-plasmon peak positions in the experimental results, and indicate the agreement between the peak positions in the experimental results and the calculated angular profiles. A four-phase-shift two-step model was used with values of the parameters indicated in the figure.

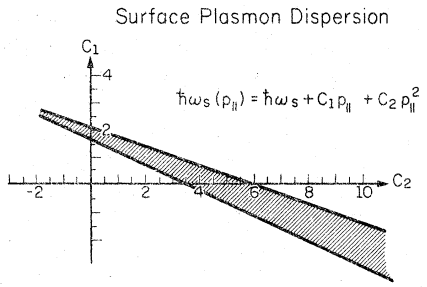

FIG. 4. Region of ambiguity in the surface-plasmon dispersion relation of Al (111) [see, e.g., Eq. (1) in the text]. Any dispersion relation whose coefficients lie in the shaded region yields a good theoretical description of the observed loss and angular profiles. The calculations were performed using the two-step model with four phase shifts derived from Snow's APW potential for the (00) beam of electrons with an inner potential $V_0 = 14.7$ eV, mean free path $\lambda_{ee} = 6$ Å, and damping $\Gamma_s = 1.4 + 0.74\, p_{\parallel}$. The loss and angular profiles used in the analyses were obtained for incident energies $E = 50$ and 60 eV with $\theta = 15°$ and $\psi = 60°$. The grid sizes in the angular and loss profiles used to construct the particular region of ambiguity shown in this figure are $\delta w = 400$ meV and $\delta\theta' = 2°$.

persion relations in that family. We divide the analysis into two parts. In this section we study the ideal resolution case. The discussion of the effects of finite resolution is given in Sec. V.

A. "Distinguishability" Grid Size: Loss Profiles

To examine the grid size required to distinguish between the loss profiles associated with various SPDR's characterized by the shaded region in Fig. 4, we present in Figs. 5–7 sample calculations of the loss profiles of the (00) beam of electrons scattered from Al (111) for the three angles of exit ($\theta' = 16° \pm 6°$, bracketing the specular direction) for two representative dispersion relations the coefficients of which lie inside the region of ambiguity shown in Fig. 4. The calculations were performed using the four-phase-shift two-step kinematical model with a fine grid of 0.050 eV of the loss energy w. The peak positions corresponding to the two SPDR's are separated by 50 meV or more for both primary energies ($E = 50$ and 60 eV, bracketing a peak in the elastic profile). Hence a grid size of $\delta w = 50$ meV permits a substantial reduction in the volume of the region of ambiguity shown in Fig. 4. Presumably a smaller value of δw would reduce this volume still further. The next question, therefore, is how small can δw be.

B. Dynamical Effects

The above calculations were performed using the two-step model in which contributions from the two lowest-order diagrams describing both elastic and energy-loss processes are added coherently. In the complete scattering theory,[11] this model corresponds to the evaluation of the diagrams shown in Figs. 8(a) and 8(b) for the cases of diffraction before loss (DL) and the loss before diffraction (LD), respectively. Dynamical (i.e., multiple scattering) processes in which the electron has scattered elastically from the lattice an arbitrary number of times, but has undergone only a single-loss event, introduce a limitation concerning the use of the two-step model.[16] It is convenient to divide the diagrams contributing to the dynamical scattering cross sections of ILEED into three classes. First, we sum all of the diagrams in which one or more elastic scattering events occur before the loss process. The sum of these diagrams defines a generalized diffraction-before-loss

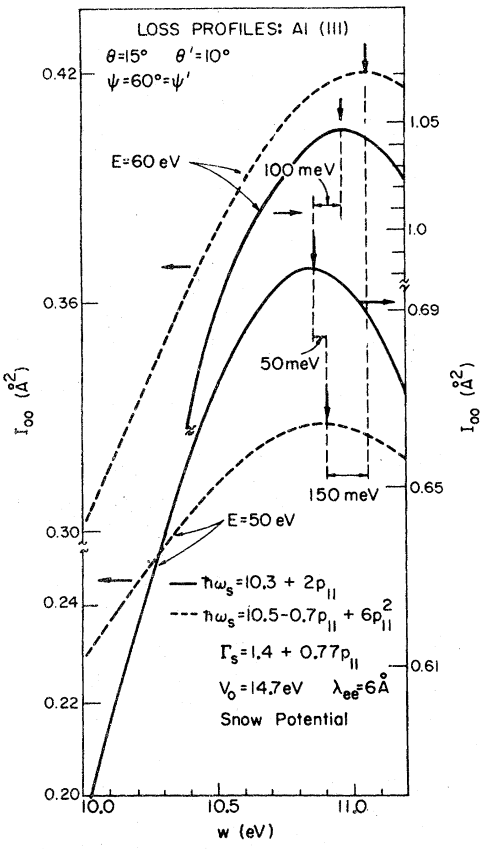

FIG. 5. Loss profiles associated with an exit angle of $\theta' = 10°$ for the (00) beam of electrons scattered from Al (111) for two dispersion relations the coefficient of which lie in the region of ambiguity shown in Fig. 4. Results of the calculations for $E = 60$ (top) and $E = 50$ eV (bottom) are given. A four-phase-shift two-step model was used with the values of parameters indicated in the figure. Vertical arrows indicate the positions of the peaks. Dashed vertical lines indicate the separations between peak positions. Shifts of 50 meV (or more) between the positions of peaks at a fixed primary-beam energy and of ~150 meV corresponding to different primary-beam energies are indicated.

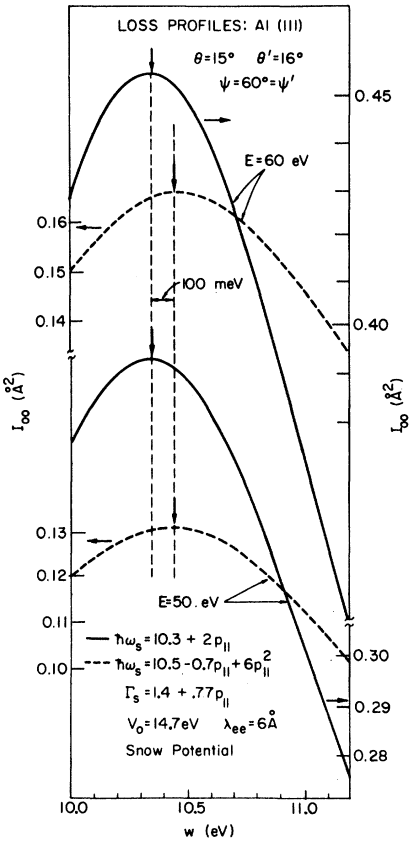

FIG. 6. Loss profiles associated with an exit angle of $\theta' = 16°$ for the (00) beam of electrons scattered from Al (111) for two dispersion relations the coefficients of which lie in the region of ambiguity shown in Fig. 4. Results of the calculations for $E = 60$ (top) and $E = 50$ eV (bottom) are given. A four-phase-shift two-step model was used with the values of the parameters indicated in the figure. Vertical arrows indicate the positions of the peaks. Dashed vertical lines indicate the separations between peak positions. Shifts of 100 meV between the positions of peaks at a fixed primary-beam energy are indicated. Since the exit direction is close to the specular direction, no shift is expected for the peak positions corresponding to different primary-beam energies.

(DL) process, indicated diagrammatically in Fig. 8(c). Second, we sum all of the diagrams in which one or more elastic scatterings occur after the loss event. This sum defines a generalized loss-before-diffraction (LD) process indicated diagrammatically in Fig. 8(d). Finally, we sum all of the diagrams in which the incident electron experiences one or more elastic scatterings *both* before and after the loss event. The sum of these diagrams defines a generalized diffraction followed by loss followed by diffraction (DLD) process indicated in Fig. 8(e). The final expressions for the dynamical ILEED cross sections given in Eqs. (23)–(41) of the first of Refs. 16 were used in an analysis of the consequencies of such "dynamical effects." Sample results are presented in Fig. 9. In this figure we compare the kinematical and dynamical loss profiles corresponding to the quadratic dispersion relation for $E = 50$ and 60 eV. A peak shift of 50 meV between the two is observed for the lower energy. Since the separation of the peaks corresponding to different dispersion relations in the loss profiles is ~ 50–100 meV (using a 50-meV grid mesh for the abscissa; see, e.g., Figs. 5–7), we conclude that given the present knowledge of the electron-solid force law, dynamical effects set a lower limit on the grid sizes useful in two-step model calculations by introducing intrinsic uncertainties of ~ 50 meV in the loss profiles (and ~ 1° in the angular profiles[16]).

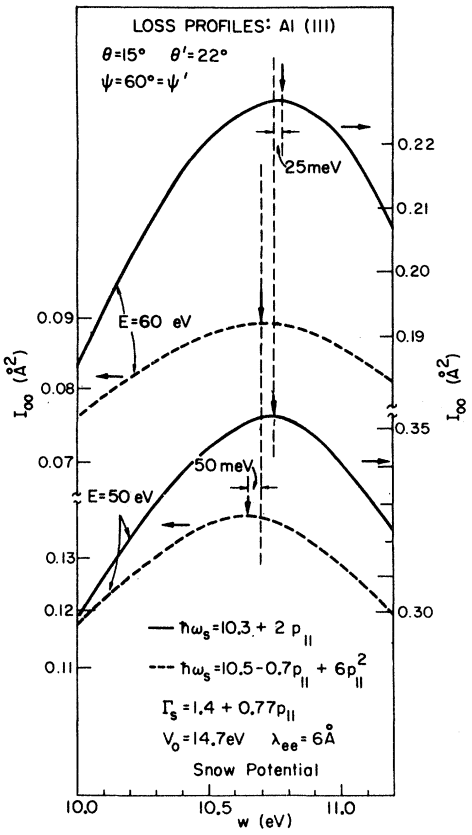

FIG. 7. Loss profiles associated with an exit angle of $\theta' = 22°$ for the (00) beam of electrons scattered from Al (111) for two dispersion relations the coefficients of which lie in the region of ambiguity shown in Fig. 4. Results of the calculations for $E = 60$ (top) and $E = 50$ eV (bottom) are given. A four-phase-shift two-step model was used with the values of the parameters indicated in the figure. Vertical arrows indicate the positions of the peaks. Dashed vertical lines indicate the separations between peak positions. Shifts of ~ 50 meV between the positions of peaks at a fixed primary-beam energy and of ~ 100 meV of the positions of the peaks corresponding to different primary-beam energies are indicated.

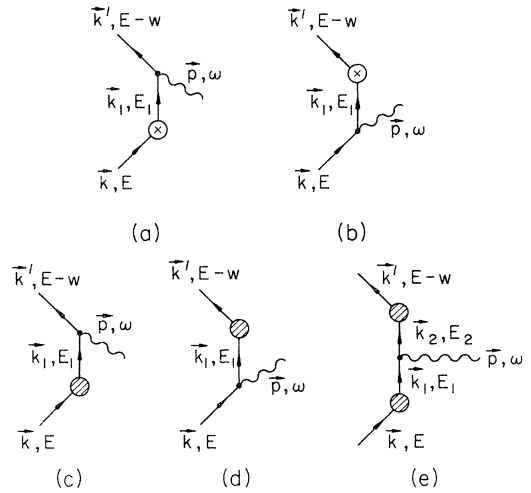

FIG. 8. Diagrams contributing to the scattering amplitudes of ILEED: (a) two step, diffraction before loss; (b) two step, loss followed by diffraction ; (c) multiple elastic diffraction before loss; (d) loss followed by multiple elastic diffraction; (e) multiple elastic diffraction both before and after loss. The perturbation-theory definition of the expressions for the cross sections associated with these diagrams is given by Duke and Laramore (Ref. 11). The shaded circle indicates the summation of an arbitrary number of individual elastic scattering events (Ref. 16) [designated by the circled cross in Figs. 8(a) and 8(b)].

C. Dependence on Diffraction Conditions

Another important question is how sophisticated a model of the ILEED process must be used to extract surface-excitation dispersion relations from measured intensities. We have argued that to within an uncertainty of $\Delta w \sim 50$ meV, the use of a two-step "kinematical" model is as adequate as that of a complete dynamical calculation, *provided we analyze only the loss profiles*. This raises the question of whether or not we can go one step further to obtain the surface excitation dispersion relation *solely from the conservation laws*[18,25]

$$w = \hbar\omega_s(\vec{p}_{\parallel}), \tag{9a}$$

$$\vec{p}_{\parallel} = \vec{k}_{\parallel} - \vec{k}'_{\parallel} - \vec{g} \ , \tag{9b}$$

without the intermediary of any microscopic theory at all. Such a determination requires that in the case of surface excitations [i.e., $\hbar\omega_s(\vec{p})$ depends only on $\vec{p}_{\parallel}$] the loss energy of the peak in the loss profile be *independent of the elastic diffraction conditions* (i.e., E, θ, ψ, θ', ψ').

In order to determine whether Eqs. (9) suffice to determine surface-excitation dispersion, we compare peak positions at the two primary energies of 50 and 60 eV for the loss profiles shown in Figs. 5–7. Diffraction phenomena in the *elastic* vertex cause shifts $\Delta w \sim 0.1$ eV which are larger than those that differentiate between the two SPDR's. This result clearly indicates that a line-shape analysis based on a microscopic model is required to extract precise surface-excitation dispersion relations. Moreover, analytical methods based on the conservation laws alone, such as that proposed by Porteus,[18,25] introduce unnecessarily large uncertainties into the resulting "dispersion relations."

D. Angular Profiles

Having established criteria for distinguishability in the loss profiles, we next examine the angular profiles. In Fig. 10 we present the angular profiles for three values of the loss energy spanning the surface-plasmon loss in Al (111), with a grid-size of 0.2° of the exit angle. The shifts in peak positions increase with increasing loss energy. However, three major obstacles occur in analyz-

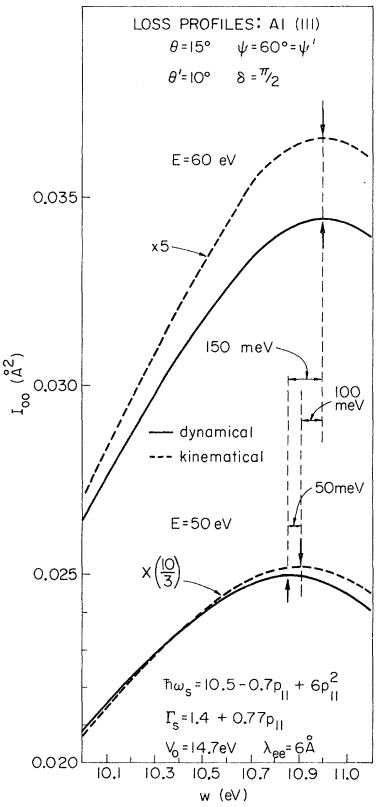

FIG. 9. Comparison between kinematical and dynamical loss profiles associated with an exit angle $\theta' = 10°$ for the (00) beam of electrons scattered from Al (111) at two incident energies, $E = 60$ (top) and $E = 50$ eV (bottom). The calculations were performed using the s-wave version of the inelastic-collision model using the parameters indicated in the figure. Vertical arrows indicate the positions of the peaks. Vertical dashed lines indicate the shifts in the positions of the peaks both for a given incident-beam energy (0 and 50 meV at 60 and 50 eV, respectively) and for different incident-beam energies.

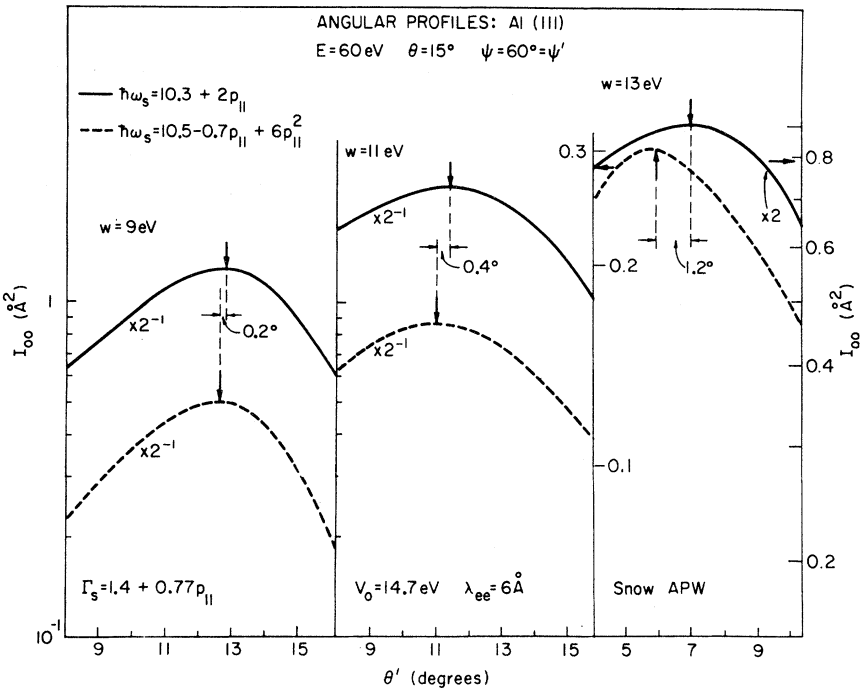

FIG. 10. Angular profiles for the (00) beam of electrons scattered from Al (111) for three values of the loss energy (w) for a primary-beam energy $E = 60$ eV. Comparison of the profiles corresponding to two dispersion relations is shown. Vertical dashed lines indicate separation of the positions of the peaks. A four-phase-shift two-step model was used with the parameters indicated in the figure.

ing the angular profiles.

(i) The grid size enabling a clear differentiation between different dispersion relations, i.e., $\delta\theta' \lesssim 1°$, is difficult to achieve experimentally.

(ii) Dynamical effects are more prominent in the angular profiles than in the loss profiles. They introduce an uncertainty $\Delta\theta' \sim 1°$ in the peak angle.[16]

(iii) For higher values fo the loss energy the surface plasmons do not lead to distinguishable loss peaks (because of their short lifetime). Thus consideration of values of $|\theta' - \theta| \gtrsim 8°$ (for the specular beam) does not reduce further the uncertainty in the dispersion relations.

Because of these effects, we base our analysis on the study of the loss profiles alone and do not examine the angular profiles further.

V. REDUCTION OF SURFACE-EXCITATION AMBIGUITY: FINITE RESOLUTION

The results presented in Sec. IV were constructed assuming ideal resolution. A critical issue in formulating a procedure for the use of a theoretical model to extract physical quantities (surface-excitation dispersion relations in our case) from experimental data is the correlation between the model calculations and the experimental procedure and uncertainties (absolute experimental uncertainties and instrumental resolution). The latter effect can be included in the model calculation procedure by convoluting the theoretical predictions with a function representing the experimental resolution. In view of the fine grid size necessary to achieve distinguishability between peak positions associated with different SPDR's, we address ourselves to the question: How important are the effects of the actual experimental resolution on the results derived in Sec. IV for the ideal (infinite) resolution case? We respond to it by examining an average over our previously predicted intensities. For each value of w the average intensity was calculated using a five-point (equally spaced) Simpson-rule integration over the interval from $w - dw$ eV to $w + dw$ eV which was then divided by the integration interval. In the figures we use the notation $\Delta w = 2dw$ for the width of the interval over which the average is taken. The same averaging procedure was performed for the angular parameter in the interval $[\theta' - d\theta', \theta' + d\theta']$. For the measurements analyzed by us[17,18] (see Sec. III), $dw = 0.5$ eV and $d\theta' = 1°$.

In Figs. 11 and 12 we compare ideal-resolution loss profiles for the two representative dispersion relations for two primary energies ($E = 50$ and 60 eV) and for two angles of exit ($\theta' = 10°$ and 22°) with their finite-resolution (averaged, $dw = 0.5$ eV, $d\theta' = 1°$) analogs. This comparison reveals that the combined effects of large energy ($\Delta w \sim 1$ eV) and angular ($\Delta\theta' \sim 2°$) resolutions do not shift peak positions in the loss profiles even on the fine grid of $\delta w = 0.050$ eV.

In addition, in Fig. 13 we compare the ideal-resolution loss profiles associated with one of the dispersion relations for a primary energy $E = 50$ eV and for three angles of exit with their finite-resolution analogs. Two sets of averaging parame-

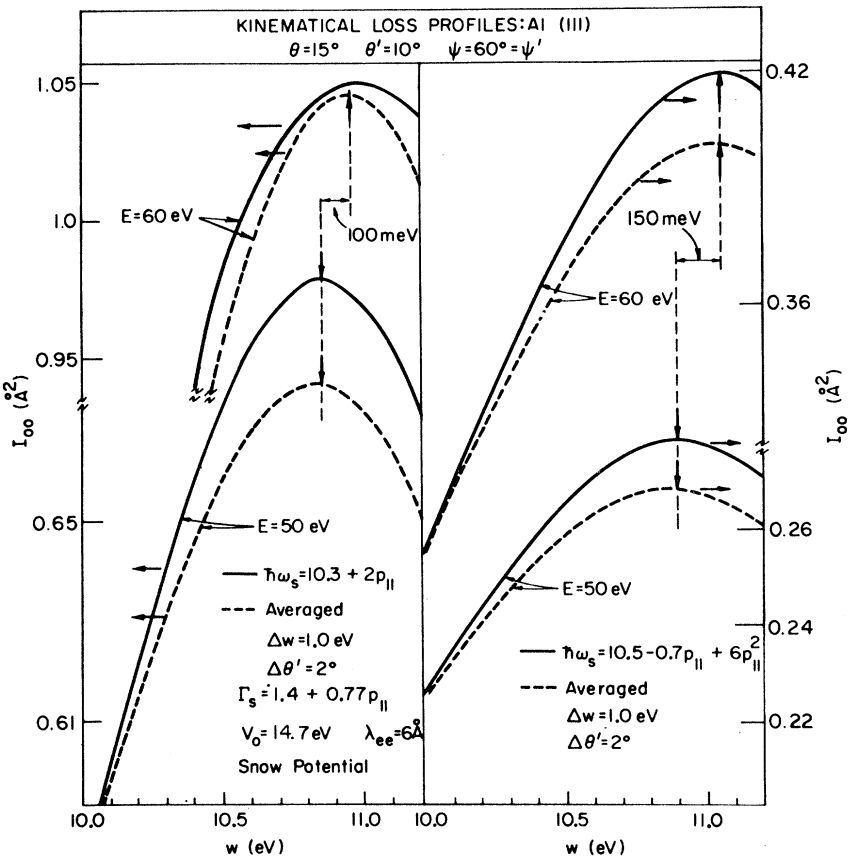

FIG. 11. Comparison of infinite-resolution (solid curves) and finite-resolution (dashed curves) loss profiles associated with an exit angle $\theta' = 10°$ for the (00) beam of electrons scattered from Al (111). Results of calculations using a four-phase-shift two-step model with two different dispersion relations (left and right panels) and two primary-beam energies, $E = 60$ (top) and $E = 50$ eV (bottom) are shown. The values of the parameters used are given in the figure. Vertical arrows indicate the positions of the peaks, and vertical dashed lines are drawn for ease in determining shifts in the positions of the peaks. As indicated, only shifts due to changes in diffraction conditions are observed. The averaging was performed using a procedure corresponding to the experimental one. For each value of w the intensity was calculated using a five-point (equally spaced) Simpson rule in the interval from $w - 0.5$ eV to $w + 0.5$ eV, which was then divided by the integration interval. The same averaging procedure was performed over the exit angle in the interval $[\theta' - 1°, \theta' + 1°]$.

ters are used to construct this figure: $dw = 0.5$ eV, $d\theta' = 1°$ (dashed curves) and $dw = 0.025$ eV, $d\theta' = 1°$ (dot-dashed curves). These results illustrate the negligible effect that almost any reasonable detector resolution has on the positions of the peaks in the loss profiles.

Another important instrumental effect is the finite angular width $\Delta\theta$ of the incident beam as it strikes the sample. In typical experiments,[18,25] $\Delta\theta \lesssim 1°$. The consequences of averaging the $\theta' = 10°$ loss profiles over (square) incident-angle distributions of various widths ($\Delta\theta$) are shown in Fig. 14. As expected, this average introduces minor alterations in the shape of the loss profiles, but no shift in the energy of the loss peak.

Finally, for the sake of completeness, we show in Fig. 15 the results obtained by averaging the $\theta' = 10°$ loss profiles over both the initial beam angular divergence $\Delta\theta \sim 1°$ and detector angular resolution $\Delta\theta' \sim 1°-2°$.

The effect of combined averages over both $\Delta\theta \sim \Delta\theta' \sim 1°$ and $\Delta w \sim 1$ eV is to broaden the ideal-resolution line shapes. Indeed the use of even larger values of $\Delta\theta \sim \Delta\theta' \sim 2°-3°$ does not perceptibly shift the energies of the peaks in the loss profiles on our energy scale of 50 meV. Therefore, useful data can be taken using grids much finer than the angular and energy resolutions of the measuring instrument. In fact, all of the conclusions drawn in Sec. IV hold equally well in cases characterized by typical experimental uncertainties.

VI. PHONON-ASSISTED DIFFRACTION

One last mechanism exists that can spoil the results of our analysis: the emission of phonons by the electron when it scatters from the ion-core potentials in the solid. The effects of electron energy loss to phonons usually are insignificant because typical metallic phonon energies are negligible ($\hbar\omega_{ph} \sim 10$ meV) relative to typical $\Delta w \sim 1$ eV loss-energy resolutions. The phonons do, however, destroy the simple parallel momentum condition (9b) by inserting additional phonon momenta on the right-hand side of this equation. In this section we argue that although in principle this effect could be severe, in practice phonon-assisted diffraction either causes an incoherent background (which can be subtracted out) or augments the "effective" instrumental angular widths by $\Delta\theta_{ph}$, $\Delta\theta'_{ph} \sim 1°$, or less. In any of these cases, the conclu-

sions drawn in the preceding sections remain unaffected.

Our entire analysis is based on an examination of the detailed behavior of clearly defined maxima in the angular profiles (fixed E, w, θ, and variable θ') in the vicinity of the elastically diffracted beams. These inelastic diffraction beams are clearly evident in Porteus's data.[18,25] They are superimposed, however, on an incoherent background which decreases with increasing θ' for fixed values of E, θ, and w. The theoretical loss and angular profiles shown in Figs. 2 and 3 are evaluated by adding to the cross sections given by Eq. (8) an incoherent background of the form

$$\left(\frac{d\sigma}{d\Omega}\right)_{\text{incoh}} = \frac{A(E,w,\theta)}{\theta' + \theta_0(E,w,\theta)} . \tag{10}$$

The parameters A and θ_0 are obtained by phenomenologically fitting the background intensity in the *angular* profiles away from the prominent diffraction maxima (i.e., beams). Therefore, to the extent that phonon-assisted diffraction contributes to this incoherent background, it has been eliminated from the data analysis. Unfortunately, the temperature dependence of this incoherent scattered intensity has not been examined experimentally. Therefore its microscopic origin is unknown. The variability of the background intensities from one sample to another, however, suggests that surface morphology, not phonon-assisted scattering, is their predominant cause.

We evaluate the consequences of phonon emission within the framework of the two-step model by following Duke and Laramore's theory[26] of phonon-assisted diffraction at the electron–ion-core "elastic" vertices. The details of the calculation of the

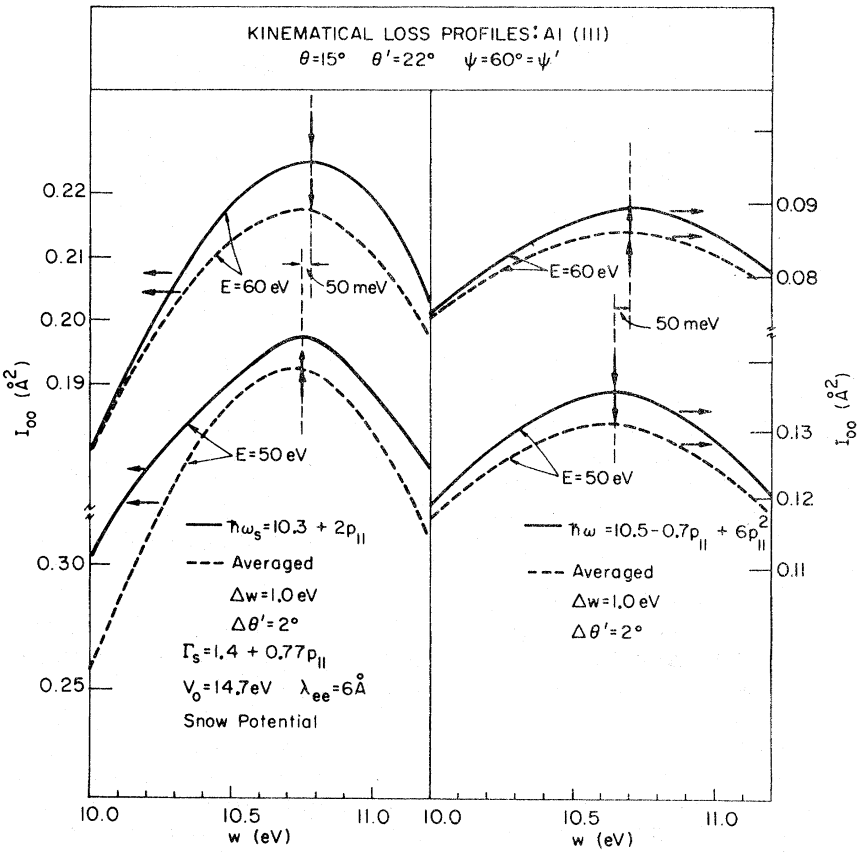

FIG. 12. Comparison of infinite-resolution (solid curves) and finite-resolution (dashed curves) loss profiles associated with the exit angle $\theta' = 22°$ for the (00) beam of electron scattered from Al (111). Results of calculations using a four-phase-shift two-step model with two different dispersion relations (left and right panels) and for two primary energies, $E = 60$ (top) and $E = 50$ eV (bottom), are shown. The values of the parameters used are given in the figure. Vertical arrows indicate the positions of the peaks, and vertical dashed lines are drawn for ease in determining shifts in the positions of the peaks. As indicated, only shifts due to changes in diffraction conditions are observed. The averaging was performed using a procedure corresponding to the experimental one. For each value of w the intensity was calculated using a five-point (equally spaced) Simpson-rule integration over the interval $[w - 0.5$ eV, $w + 0.5$ eV$]$, which was then divided by the integration interval. The same averaging procedure was performed over the exit angle in the interval $[\theta' - 1°, \theta' + 1°]$.

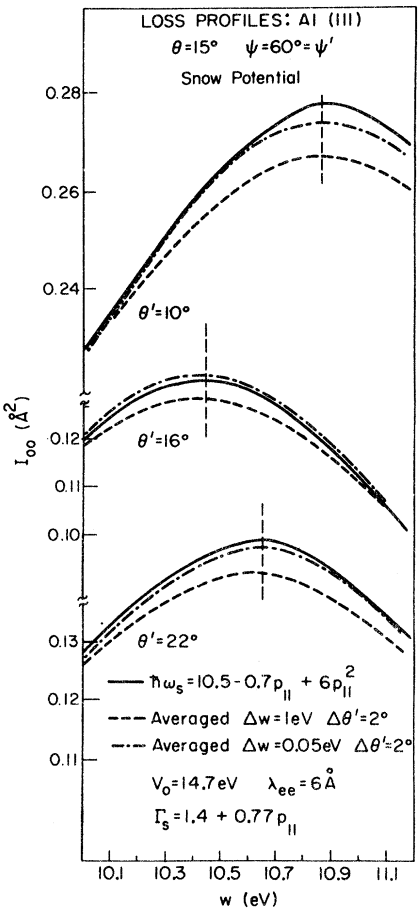

FIG. 13. Comparisons of infinite-resolution (solid curve) and finite-resolution loss profiles associated with the exit angles ($\theta' = 10°$, 16°, and 22°) for the (00) beam of electrons of incident energy $E = 50$ eV scattered from Al (111). The finite-resolution profiles were obtained by using the averaging procedure described in the caption to Fig. 11 for two sets of averaging intervals $dw = 0.5$ eV, $d\theta' = 1°$ (dashed curves) and $dw = 0.025$ eV, $d\theta' = 1°$ (dot-dashed curves). Vertical dashed lines were drawn for ease in determing the positions of the peaks. As is indicated,no shift in the postions of the peaks is observed between the ideal- and finite-resolution results for any of the three angles of exit (bracketing the specular direction). The calculations were performed using a four-phase-shift two-step model with the dispersion relation and parameters indicated in the figure.

quasielastic scattering cross sections, i.e.,

$$\left(\frac{d\sigma}{d\Omega}\right)_{qe} = \int_{E-\Delta w}^{E+\Delta w} \left(\frac{d^2\sigma}{d\Omega d\epsilon}\right) d\epsilon, \tag{11}$$

are given in the Appendix. The quantity Δw is the range of loss energy averaged over by the instrument. Our analysis is based on the assumption that Δw (~1 eV) is much larger than typical phonon energies ($\hbar\omega_{ph} \sim 10$ meV). Phonon-assisted diffraction has been discussed recently in the literature also

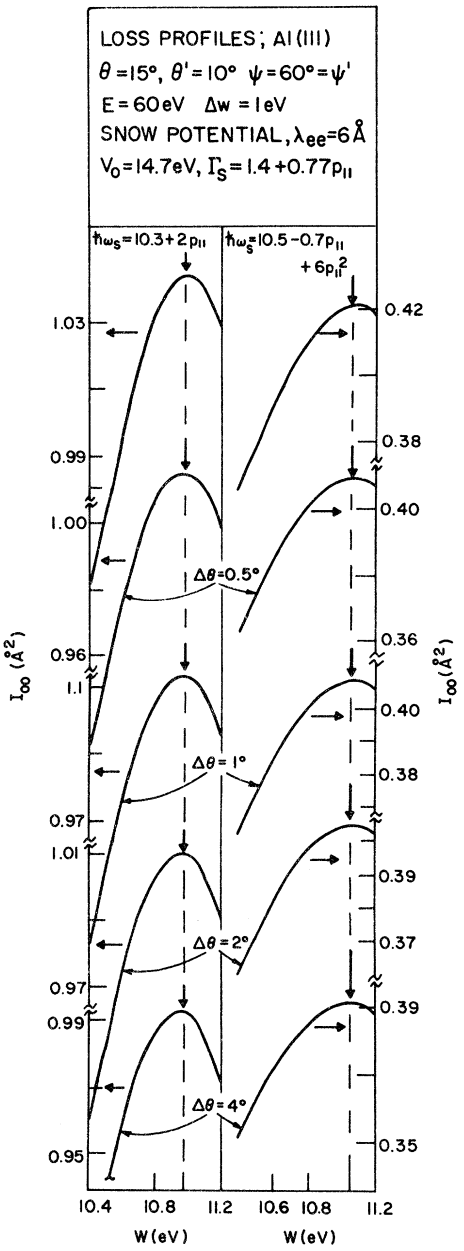

FIG. 14. Comparison of infinite-resolution and finite-resolution loss profiles associated with an exit angle $\theta' = 10°$ for the (00) beam of electrons scattered from Al (111). Results of calculations using a four-phase-shift two-step model with two different dispersion relations (left and right panels) at the primary-beam energy $E = 60$ eV are shown. The values of the parameters used are given in the figure. Vertical arrows indicate the positions of the peaks, and vertical dashed lines are drawn for ease in determining shifts in the positions of the peaks. The averaging was performed using a procedure corresponding to that for the exit angle. For each value of w the intensity was calculated using a five-point (equally spaced) Simpson rule in the interval $[w - 0.5$ eV, $w + 0.5$ eV$]$, which was then divided by the integration interval. The same averaging procidure was performed over the entrance angle in the interval $[\theta - \frac{1}{2}\Delta\theta,\ \theta + \frac{1}{2}\Delta\theta]$.

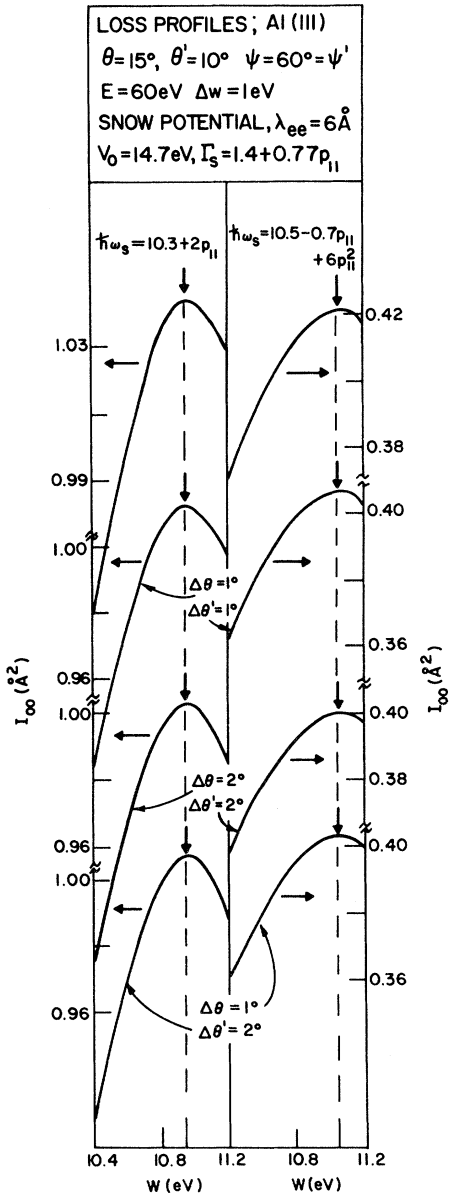

FIG. 15. Comparison of infinite-resolution and finite-resolution loss profiles associated with an exit angle $\theta' = 10°$ for the (00) beam of electrons scattered from Al (111). Results of calculations using a four-phase-shift two-step model with two different dispersion relations (left and right panels) at the primary-beam energy $E = 60$ eV are shown. The values of the parameters used are given in the figure. Vertical arrows indicate the positions of the peaks, and vertical dashed lines are drawn for ease in determining shifts in the positions of the peaks. The averaging was performed using a procedure corresponding to that used earlier. For each value of w the intensity was calculated using a five-point (equally spaced) Simpson rule in the interval $[w-0.5\,\text{eV}, w+0.5\,\text{eV}]$, which was then divided by the integration interval . The same averaging procedure was performed over the exit angle in the interval $[\theta' - \frac{1}{2}\Delta\theta', \theta' + \frac{1}{2}\Delta\theta']$ and the entrance angle in the interval $[\theta - \frac{1}{2}\Delta\theta, \theta + \frac{1}{2}\Delta\theta]$.

by several other authors[26-32] in whose papers complete references to earlier work may be found.

In the Appendix we examine the emission of two types of phonons at the quasielastic electron–ion-core vertices: Einstein phonons described by the dispersion relation

$$\hbar\omega_{ph}(\vec{p}) = \hbar\omega_0 \tag{12a}$$

and Debye phonons described by the dispersion relation

$$\hbar\omega_{ph}(\vec{p}) = \hbar v_\lambda p, \tag{12b}$$

in which $v_\lambda \sim 10^5$ cm/sec for both longitudinal ($\lambda = 1$) and transverse ($\lambda = 2, 3$) phonons. Emission of surface phonons changes only the value of numerical constants used in the model analysis.[27] The use of a discrete-lattice model[32] rather than an elastic-continuum model[27] of the phonon spectra has, thus far, led to different results for acoustical phonons because the finite slabs used in the numerical calculations do not provide enough long wavelength phonon modes normal to the slab. Available experimental data[29-31] agree only with the predictions of the elastic-continuum model.

Our examination of the Born-approximation description of the emission and/or absorption of phonons at the quasielastic vertices in the two-step model leads to three important conclusions. First, the emission (absorption) of an arbitrary number of Einstein phonons and of two or more Debye phonons contributes only to the incoherent background intensity. Second, the emission (absorption) of a single Debye phonon causes a contribution to the scattered intensity which diverges for scattering in the elastic specular direction as $|\vec{k}_{\parallel}' - \vec{k}_{\parallel}|^{-1}$ or $\ln|\vec{k}_{\parallel}' - \vec{k}_{\parallel}|$ in the high- ($\kappa T \gtrsim \hbar\omega_m$) and low- ($\kappa T \ll \hbar\omega_m$) temperature limits, respectively. The $\hbar\omega_m \sim 10$ meV is the maximum acoustical phonon energy. Third and finally, the emission of two Debye phonons diverges as $\ln|\vec{k}_{\parallel}' - \vec{k}_{\parallel}|$ in the high-temperature limit but contributes to a relatively uniform (i. e., incoherent) background in the low-temperature limit.

These three results illustrate an important fact: Phonon-assisted diffraction either is strongly peaked in the elastic-specular direction or else is nearly uniformly spread over momentum space. In the latter case (e.g., Einstein phonon, multiple Debye phonon emission), the phonon-assisted contributions to the ILEED intensities are eliminated from our analysis via the background subtraction procedure [i.e., Eq. (10)]. In the former case, they act as a beam-broadening mechanism in θ (diffraction before loss) or θ' (loss before diffraction). Experimentally, the beam broadening is known to be $\Delta\theta' \sim \Delta\theta' \sim 1° - 2°$.[28-31] We demonstrated explicitly in Sec. V, however, that beam broadening mechanisms do not affect our extraction of surface-

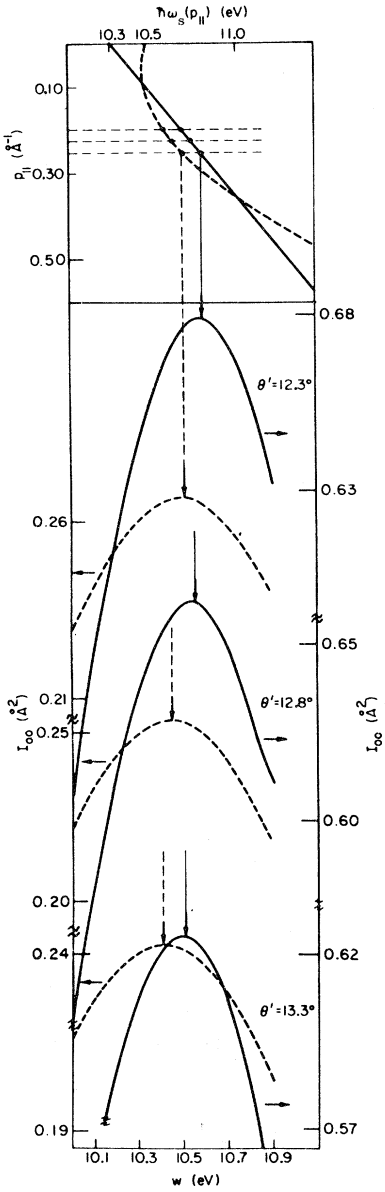

FIG. 16. Schematic indication of a procedure to reduce the uncertainty in the determination of the surface-plasmon dispersion relation. In the top panel two dispersion relations (dashed and solid lines) are shown. The horizontial dashed lines indicate a region of maximum difference between the two dispersion relations (i.e., at exit-beam angles θ_m and $\theta_m \pm 0.5°$). In the lower panel, loss profiles for the (00) beam of electrons scattered from Al (111) for two dispersion relations are shown. Three sets of results are shown corresponding to the three horizontal dashed lines in the top panel. Vertical arrows indicate positions of the peaks. Distinguishability is clearly observed in all three peaks. The calculations were performed for an incident electron energy of 50 eV using the four-phase-shift two-step model with the parameters $\theta = 15°$, $\psi = \psi' = 60°$, $V_0 = 14.7$ eV, $\lambda_{ee} = 6$ Å. The two plasmon dispersion relations are given by $\Gamma_s(p_\parallel) = 1.4 + 0.77\ p_\parallel$, $\hbar\omega_s(p_\parallel) = 10.3 + 2p_\parallel$ (solid line), and $\hbar\omega_s(p_\parallel) = 10.5 + 0.7\ p_\parallel + 6p_\parallel^2$ (dashed line).

plasmon dispersion from the ILEED loss profiles. Thus phonon-assisted diffraction does not influence our conclusions in any significant way. This analysis reveals, moreover, that the diffuse-Einstein and multiple-Debye-phonon emission and absorption processes remove electrons from the coherent incident and scattered beams. Therefore, these processes (but *not* the beam broadening ones) act to produce a temperature-dependent contribution to the elastic one-electron optical potential [i.e., V_0 and λ_{ee} in Eqs. (2)]. We have avoided explicit consideration of this contribution by taking V_0 and λ_{ee} directly from the *elastic* LEED intensity data to use in the analysis of the corresponding ILEED data.

VII. PROCEDURE FOR EXTRACTION OF SURFACE-EXCITATION DISPERSION RELATIONS VIA ILEED

As a consequence of the results presented above we have formulated a multiple-step procedure for the extraction of surface excitation dispersion relations via ILEED. This procedure is economical in both measurements and analysis while enabling a substantial reduction of the uncertainties in the resulting excitation dispersion relation relative to those accompanying the initial analyses of surface-plasmon dispersion at Al (111).[13–15] The procedure consists of the following steps: (a) Locate several prominent peaks (of energy $E = E_p$) in the elastic energy profiles for various incident-beam parameters (E, θ, ψ). (b) Measure and analyze loss profiles at $E = E_p$, $E_p \pm \hbar\omega_s$ eV using a coarse grid $\delta w = 0.4$ eV, $\delta\theta' = 2°$. Bound the domain of parameter uncertainty in Eqs. (7) on this basis (see, e.g., Fig. 4). (c) Examine the data and parameter uncertainty, and select small regions in which good data exist and the peak positions in the loss profiles are sensitive functionals of the surface-excitation dispersion and damping. In these regions take and analyze data on the fine grid $\delta w \sim 0.050$ eV and $\delta\theta' \sim 0.5°$.

An example of distinguishing between two Al (111) SPDR's using such a fine grid is shown in Fig. 16. Inspection of the top panel shows three regions of $p_\parallel$ (corresponding to three regions of exit angles) in which the two SPDR's are most distinguishable. The region of small $p_\parallel$ corresponds to angles of exit near the specular directions and consequently is not useful. In the region of large $p_\parallel$ surface-plasmon damping dominates. Hence we examine the middle (dashed) region. In view of a possible error in the absolute value of the exit angle (θ') of $\sim 1°$, we have calculated the loss profiles for the two dispersion relations for values of the exit angle θ'_m and $\theta'_m \pm 0.5°$, where θ'_m is the angle corresponding to the value of $p_\parallel$ for which the separation between the dispersion relations is maximal. It is evident that distinguishability by

100 meV and more is predicted for all angles in the region of maximum sensitivity. Use of the above procedure permits us to reduce the uncertainties in Eq. (1) by a factor of about 4, i.e.,

$$\hbar\omega_s(p_\parallel) = \hbar\omega_s(\pm 0.050\ \text{eV}) + C_1(\pm 0.7)p_\parallel + C_2(\pm 1.2)p_\parallel^2 . \tag{13}$$

The ultimate determination of the surface-excitation dispersion and damping is based upon using such a fine-grid analysis for incident-beam parameters (E, θ, ψ) associated with several prominent resonances in the elastic energy profiles. The regions of ambiguity associated with the various elastic resonances overlap but are not identical.[17] This overlap both assures us that systematic errors in the parametrization of the elastic electron–ion-core vertices are not overwhelming and permits us to reduce further the uncertainty in the surface-excitation dispersion relation.

Summarizing, we have extended earlier analyses[13–15] of surface excitation dispersion via ILEED by examining systematically the sources of theoretical and instrumental error in the analytical procedure. We find that the two-step model of ILEED constitutes a necessary and sufficient level of description of the inelastic scattering process *provided we confine our analysis to loss profiles using a loss-energy grid* $\delta w > 0.050\ eV$. Neither reasonable instrumental resolutions ($\Delta w \sim 1$ eV, $\Delta\theta \sim 1°-3°$, $\Delta\theta' \sim 1°-3°$) nor phonon-assisted-diffraction processes affect the energies of the peaks in the loss profiles *on this loss-energy scale*. Based on these results, we propose a practical yet accurate procedure for determining surface-excitation dispersion relations from measured ILEED intensities.

ACKNOWLEDGMENTS

The authors are indebted to Bob McFarlane and Jack Gladdin for unusually extensive and prompt assistance in preparing the figures, and to Dr. J. O. Porteus for numerous helpful discussions and the data in the sample analysis of surface-plasmon dispersion on Al (111).

APPENDIX

In this appendix we discuss the probability of (multiple) phonon emission at the elastic scattering vertex in the two-step model of ILEED. Following a recapitulation of the necessary general formulas, we show that an Einstein model of the phonon spectrum predicts that phonon-assisted quasielastic scattering events contribute only to the incoherent background (i.e., not to the coherently diffracted beams). We conclude by demonstrating that a Debye model of the phonon spectrum leads to an infrared catastrophe in the quasielastic scattering cross section so that the emission of Debye phonons can be interpreted as the broadening of the zero-phonon δ function in momentum space into a beam of finite angular width, $\Delta\theta' \sim 1°$.

Our starting point is the expression given by Duke and Laramore[26] for the quasielastic single-scattering cross section of an electron from a vibrating lattice [Eq. (49) in Ref. 26]:

$$\left(\frac{d\sigma}{d\Omega}\right)^{(2)}_{\mathbf{q}\mathbf{e}} = \left| \frac{m v_q}{2\pi\hbar^2}\, e^{-W(\vec{q})} \right|^2 \times \sum_{l,m} e^{-i\vec{q}\cdot(\vec{R}_m - \vec{R}_l)}\, e^{iq^\alpha D_{\alpha\beta}(l,m) q^\beta}, \tag{A1}$$

$$\vec{q} = \vec{k}' - \vec{k}, \tag{A2}$$

$$D_{\alpha\beta}(l,m) = (-i\hbar\delta_{\alpha\beta}/2M) \times \frac{1}{N}\sum_{\vec{p}} \frac{1}{\omega(\vec{p})} \coth\left(\frac{\hbar\omega(\vec{p})}{2\kappa T}\right) e^{i\vec{p}\cdot(\vec{R}_l - \vec{R}_m)}. \tag{A3}$$

In these equations we use $\vec{R}_m$ to designate the equilibrium position of an ion core of mass M at the site labeled by m, $\omega(\vec{p})$ to denote the dispersion relation of the phonons, α and β to indicate Cartesian components, v_q to specify the Fourier transform of the electron–ion-core interaction, and κT to indicate Boltzmann's constant times the temperature. The Debye–Waller factors are given by

$$2W_l(\vec{q}) = iq^\alpha D_{\alpha\beta}(l,l) q^\beta. \tag{A4}$$

Therefore it is evident that in the diagonal term in the sum over l and m in Eq. (A1), the $e^{iq^\alpha D_{\alpha\beta}(l,m)q^\beta}$ factor precisely cancels the $e^{-2W(\vec{q})}$ term in the prefactor. For simplicity, we are considering a model in which all of the ion cores exhibit identical vibrational amplitudes, although the analysis can easily be extended to more realistic cases without altering anything but the numerical value of the constants in our formulas.[27]

The usual approach to phonon-assisted diffraction consists[26–32] of expanding the factor $e^{iq^\alpha D_{\alpha\beta}(l,m)q^\beta}$ in Eq. (A1) and considering each term separately. The first term in the expansion (i.e., unity) is called the elastic term; the term linear in $D(l, m)$ causes "thermal diffuse" scattering; and higher-order terms in $D(l, m)$ are referred to as multiphonon terms. We see below that such an expansion is misleading for Debye phonons because terms in the series diverge.

The dispersion relation describing an Einstein-phonon spectrum is

$$\omega(\vec{p}) = \omega_0, \quad p \le p_m = (6\pi^2 n)^{1/3} \tag{A5}$$

in which n is the atomic density of the model monatomic lattice. We obtain the phonon propagator from Eq. (A3):

$$D_{\alpha\beta}(l,m) = \frac{i\hbar \coth(\hbar\omega_0/2\kappa T)\delta_{l,m}}{2M\omega_0}. \tag{A6}$$

Because the $\omega(\vec{p})$ terms are independent of $\vec{p}$, only

the diagonal term in $D(l, m)$ is nonzero. Consequently, the quasielastic scattering cross section is given by

$$\left(\frac{d\sigma}{d\Omega}\right)_{qe}^{(2)} = \left| mv_q\, e^{-W(\vec{q})}/2\pi\hbar^2 \right|^2 \times\left(N(e^{2W(\vec{q})}-1)+\sum_{l,m} e^{i\vec{q}\cdot(\vec{R}_l-\vec{R}_m)}\right). \quad \text{(A7)}$$

The second term in Eq. (A7) describes the coherent diffraction of the electron from the lattice. It is unaffected by the phonon-assisted scattering events which serve only to cause the incoherent background scattering from the total lattice of N ion cores described by the first term in Eq. (A7). *Thus Einstein phonons extract spectral density from the coherent elastic intensity and place it in a completely incoherent background which is uniformly distributed throughout the Brillouin zone.* In a term-by-term expansion of Eq. (A1), this result is reflected in the fact that the nth order terms (except that for $n=0$) depend on $\vec{q}$ only via the $[q^2]^n$ prefactors of the rigid-ion model.

The dispersion relation describing a Debye-phonon spectrum is

$$\omega_\lambda(\vec{p}) = v_\lambda p, \quad p \le p_m \quad \text{(A8)}$$

for one longitudinal ($\lambda = 1$) and two transverse ($\lambda = 2, 3$) branches. We define an average speed of sound v_s via

$$v_s^{-2} = \frac{1}{3}\sum_{\lambda=1}^{3} v_\lambda^{-2}. \quad \text{(A9)}$$

For purposes of illustration, it is convenient, but not necessary, to work in the high-temperature limit

$$\coth[\hbar\omega_\lambda(\vec{p})/2\kappa T] \cong 2\kappa T/\hbar\omega_\lambda(\vec{p}) \quad \text{(A10)}$$

for all three branches of the spectrum. In this limit

$$D_{\alpha\beta}(l, m) = (-9i\kappa T/M\omega_m^2)\delta_{lm} - (9\pi i\kappa T/2M\omega_m^2 p_m |\vec{R}_l - \vec{R}_m|)[1-\delta_{lm}], \quad \text{(A11)}$$

$$\omega_m \equiv p_m v_s. \quad \text{(A12)}$$

Therefore the emission of multiple low-energy phonons causes a R^{-1} long-range correlation between ion cores separated by a distance R. The quasielastic Born cross section is given by

$$\left(\frac{d\sigma}{d\Omega}\right)_{qe}^{(2)} = \left| mv_q\, e^{W(\vec{q})}/2\pi\hbar^2 \right|^2 \times\left(Ne^{2W(\vec{q})}+\sum_{l\neq m} e^{i\vec{q}\cdot(\vec{R}_l-\vec{R}_m)}\, e^{\alpha(\vec{q})/|\vec{R}_l-\vec{R}_m|}\right), \quad \text{(A13a)}$$

$$\alpha(\vec{q}) = \pi w(\vec{q})/2p_m. \quad \text{(A13b)}$$

A difficulty is encountered in expanding the second exponent in a power series because the terms in this series diverge. This fact may be illustrated by the familiar[27-29] case of scattering from a single layer of $N_\parallel$ ion cores. Using the identity

$$\frac{1}{|\vec{R}_l - \vec{R}_m|} = 4\pi\int \frac{d^3p}{(2\pi)^3}\,\frac{e^{i\vec{p}\cdot(\vec{R}_l-\vec{R}_m)}}{p^2} \quad \text{(A14)}$$

in Eq. (A13a), we can write

$$S(\vec{q}) = \sum_{l,m} e^{i\vec{q}\cdot(\vec{R}_l-\vec{R}_m)} \times\exp\left(4\pi\alpha(\vec{q})\int\frac{d^3p}{(2\pi)^3}\,\frac{e^{i\vec{p}\cdot(\vec{R}_l-\vec{R}_m)}}{p^2}\right) = \sum_t s_t(\vec{q}). \quad \text{(A15)}$$

The sum over t designates terms in the power-series expansion of the latter exponent in Eq. (A15). For a single layer of scatterers we obtain

$$S_0(\vec{q}) = N_\parallel(2\pi)^2 A^{-1}\delta(\vec{q}_\parallel - \vec{g}), \quad \text{(A16a)}$$

$$S_1(\vec{q}) = \frac{4N_\parallel\,\alpha(\vec{q})}{A}\sum_{\vec{g}}\frac{1}{|\vec{q}_\parallel-\vec{g}|}\,\tan^{-1}\left(\frac{p_m}{|\vec{q}_\parallel-\vec{g}|}\right), \quad \text{(A16b)}$$

$$S_2(\vec{q}) \cong \frac{2\pi N_\parallel\alpha^2(\vec{q})}{A}\sum_{\vec{g}}\ln(p_m/|\vec{q}-\vec{g}|). \quad \text{(A16c)}$$

The S_2 term is calculated presuming $|\vec{q}_\parallel - \vec{g}|$ to be small in order to isolate the divergence as $|\vec{q}_\parallel - \vec{g}| \to 0$. The higher-order S_t are convergent functions (i.e., $u^{n-2}\ln u$) of $|\vec{q}_\parallel - \vec{g}|$ when $\vec{q}_\parallel \to \vec{g}$. It is evident from Eqs. (A16), however, that the one- and two-phonon contributions to $S(\vec{q})$ both diverge as $\vec{q}_\parallel \to \vec{g}$, i.e., as a reciprocal-lattice rod is approached by varying the external-beam parameters. Because they result from an infrared catastrophe, these phonon-assisted diffraction divergences are more severe for $\kappa T > \hbar\omega_D$ than for $\kappa T \lesssim \hbar\omega_D$. In the low-temperature limit ($\kappa T \ll \hbar\omega_D$) they are reduced by one order. That is, the $S_1(\vec{q})$ is proportional to $\ln(p_m/|\vec{q}_\parallel - \vec{g}|)$. Since $S_2(\vec{q})$ is proportional to $|\vec{q}_\parallel - \vec{g}|\ln|\vec{q}_\parallel - \vec{g}|$, it converges as $\vec{q}_\parallel \to \vec{g}$.

These divergences do not disappear when multilayer diffraction is considered. In the case of the single-phonon term (i.e., thermal diffuse scattering), we obtain for $q_\parallel \ll p_m$ and $\kappa T \lesssim \hbar\omega_D$ the result

$$\left(\frac{d\sigma}{d\Omega}\right)_{qe}^{tds} = N_\parallel\left(mv_q\frac{e^{-W(\vec{q})}}{2\pi\hbar^2}\right)^2 \times\left(\frac{2\pi\alpha(\vec{q})}{Aq_\parallel}\right)\left|1-e^{[(2ik_\perp(0,E)-q_\parallel)d]}\right|^{-2} \quad \text{(A17)}$$

for the specular-beam (i.e., $\vec{q}_\parallel = \vec{k}_\parallel' - \vec{k}_\parallel$) cross section predicted by our simple model. The expected (and observed[29]) linear dependence on q^2, T, and $q_\parallel^{-1}$ all are present. A more sophisticated model of the lattice dynamics would change only the numerical constants.[27] Note that departures from the specular direction (i.e., $\vec{q}_\parallel \neq 0$) act to damp out

further, not tune, the Bragg resonance associated with coherent multilayer scattering. In practice,[28-31] either typological disorder on the surface or the $q_{\parallel}^{-1}$ factor in Eqs. (A16) and (A17) lead to a beam of angular width $\Delta\theta' \sim 1°$ when the intensities are plotted for fixed incident-beam energy as a function of the exit angle on a linear scale.

From Eqs. (A7), (A13), and (A17) we discern two types of phenomena associated with phonon-assisted diffraction. The flat higher-frequency phonon modes give rise to short-range correlations in the $D(l, m)$. These correlations extract intensity from the coherent scattering and place it in the incoherent background. The low-frequency (long-wavelength) acoustical modes introduce long-range atomic correlations which emanate from an infrared catastrophe associated with the copious emission of low-energy phonons. Such correlations lead to the broadening of the coherently diffracted electron beams, rather than the enhancement of the incoherent background intensity. Often, the instrumental angular resolution $\Delta\theta$ is wider than the phonon-induced beam broadening.[28] In this case, which is that emphasized in the text, phonon-assisted diffraction affects the absolute ILEED intensities but not our peak-position analysis. Even if the instrumental and phonon-assisted $\Delta\theta$ are comparable, our analysis is valid provided that a suitable temperature-dependent angular-averaging function is used.

---

*Research supported in part by the Air Force Office of Scientific Research, Office of Aerospace Research, USAF, under Grant No. AFOSR 71-2034, by the Advanced Research Projects Agency under Contract No. HC 15-67-C-0221, and by the Joint Services Electronics Program under Contract No. DAAB-07-67-0199. The United States Government is authorized to reproduce and distribute reprints for Governmental purposes notwithstanding any copyright notation hereon.

†Present address: Xerox Research Laboratories, Rochester, N. Y. 14644.

[1]C. B. Duke, Ann. Rev. Mater. Sci. 1, 165 (1971); C. B. Duke and R. L. Park, Physics Today 25 (No. 8), 23 (1972).

[2]R. H. Ritchie, Phys. Rev. 106, 874 (1957).

[3]E. A. Stern and R. A. Ferrell, Phys. Rev. 120, 130 (1960).

[4]P. J. Feibelman, C. B. Duke, and A. Bagchi, Phys. Rev. B 5, 2436 (1972).

[5]P. A. Fedders, Phys. Rev. 153, 438 (1967).

[6]P. J. Feibelman, Phys. Rev. 176, 551 (1968); B 3, 2974 (1971).

[7](a) See Refs. 18–24, 31, 34, cited in Ref. 4. (b) D. E. Beck and V. Celli, Phys. Rev. Letters 28, 1124 (1972).

[8]R. H. Ritchie and A. L. Marusak, Surface Sci. 4, 234 (1966).

[9]A. J. Bennett, Phys. Rev. B 1, 203 (1970).

[10]H. Kanazawa, Prog. Theoret. Phys. (Kyoto) 26, 851 (1961).

[11]C. B. Duke and G. E. Laramore, Phys. Rev. B 3, 3183 (1971).

[12]G. E. Laramore and C. B. Duke, Phys. Rev. B 3, 3198 (1971).

[13]C. B. Duke and A. Bagchi, J. Vac. Sci. Technol. 9, 738 (1972).

[14]A. Bagchi, C. B. Duke, P. J. Feibelman, and J. O. Porteus, Phys. Rev. Letters 27, 998 (1971).

[15]A. Bagchi and C. B. Duke, Phys. Rev. B 5, 2784 (1972).

[16]C. B. Duke and U. Landman, Phys. Rev. B 6, 2956 (1972); 6, 2968 (1972).

[17]U. Landman, C. B. Duke, and J. O. Porteus J. Vac. Sci. Technol. (to be published).

[18]J. O. Porteus, in Proceedings of the Thirty-Second Annual Physical Electronics Conference, Albuquerque, N. M., 1972 (unpublished).

[19]C. B. Duke and U. Landman, in *Proceedings of the Sixth LEED Seminar* (Natl. Bur. Std., Washington, D. C., 1972).

[20]C. B. Duke, J. R. Anderson, and C. W. Tucker, Jr., Surface Sci. 19, 117 (1970).

[21]C. B. Duke and C. W. Tucker, Jr., Surface Sci. 15, 231 (1969).

[22]G. E. Laramore and C. B. Duke, Phys. Rev. B 5, 267 (1972).

[23]E. C. Snow, Phys. Rev. 158, 683 (1967).

[24]C. B. Duke, A. J. Howsmon, and G. E. Laramore, J. Vac. Sci. Technol. 8, 10 (1971).

[25]J. O. Porteus and W. N. Faith, Phys. Rev. B 2, 1532 (1970); J. Vac. Sci. Technol. 9, 1062 (1972).

[26]C. B. Duke and G. E. Laramore, Phys. Rev. B 2, 4765 (1972).

[27]D. L. Huber, Phys. Rev. 153, 772 (1967). Complete references to the theoretical literature on thermal diffuse scattering may be found in this reference and in Refs. 26 and 32.

[28]E. R. Jones, J. T. McKinney, and M. B. Webb, Phys. Rev. 151, 476 (1966).

[29]J. T. McKinney, E. R. Jones, and M. B. Webb, Phys. Rev. 160, 523 (1967).

[30]R. F. Barnes, M. G. Lagally, and M. B. Webb, Phys. Rev. 171, 627 (1968).

[31]M. G. Lagally and M. B. Webb, in *The Structure and Chemistry of Solid Surfaces*, edited by G. A. Somorjai (Wiley, New York, 1969), Chap. 20.

[32]F. W. deWette and R. E. Allen, in *The Structure and Chemistry of Solid Surfaces*, edited by G. A. Somorjai (Wiley, New York, 1969), Chap. 18.